9.3 FACTORS INFLUENCING OROGRAPHIC PRECIPITATION FOR UNIFORM FLOW OVER A TWO-DIMENSIONAL MOUNTAIN: PART I. BASIC FLOW SPEED

Gökhan Sever[1] and Yuh-Lang Lin[1,2,*]
[1]Department of Energy & Environmental Systems, [2]Department of Physics
North Carolina A&T State University, Greensboro, North Carolina, USA

ABSTRACT

A series of systematic two-dimensional numerical experiments have been conducted to investigate combined effects of dynamical, thermodynamical and microphysical processes on orographic precipitation (OP) with varying incoming basic flow speed (*U*) in a conditionally unstable uniform flow. Detailed temporal and spatial evolutions of precipitation are analyzed in a much stronger *U*. The first set of the experiments are performed to verify moist flow regimes found in a previous study of Chu and Lin. In the first part of this study, two of the three regimes (I and III) of Chu and Lin have been correctly reproduced using the Weather Research and Forecasting (WRF) model. It is found that, the transient regime, which is the stationary convective precipitation over the mountain (Regime II) is sensitive to the selection of *U*. In the second part of this study, Chu and Lin's study is extended to very high Froude-number flows comparable to category 2-3 hurricane wind (50 m s^{-1}). It is found that the maximum total precipitation is linearly proportional to the *U* due to orographic lifting but the maximum hourly precipitation rate possesses no linear relation to the *U* due to highly unstable incoming flow. It is also noted that the total precipitation maximum is shifted closer to the mountain peak and lee-ward side as the *U* increases. Bi-modal precipitation distribution is obtained on the downwind side of the mountain after 12 hours of the simulation with a very high wind speed. Time and spatial accumulated distributions of hydrometeors indicate that the most dominant microphysical species is graupel in producing surface precipitation. At later stage, the system has produced cellular convective cells which are propagating upstream; however, their contribution to the precipitation is negligible.

1. INTRODUCTION

Study of orographic precipitation (OP) formation and evolution in terms of orographic forcing and atmospheric instabilities poses an interesting, yet not well understood, problem in mesoscale meteorology. In order to improve the understanding of the problem, one of the approaches is to make idealized simulations with mesoscale numerical models. Idealized simulations of the formation and evolution of OP have been actively studied for the past two decades (Chu and Lin 2000 – hereafter referred to as CL00, Colle 2004, Chen and Lin 2005, Chen et al. 2008, Miglietta and Rotunno 2009, Miglietta and Rotunno 2010, and Miglietta and Rotunno 2014 among others).

* *Corresponding author address*: Dr. Yuh-Lang Lin, 302H, Gibbs Hall, North Carolina A&T State University, Greensboro, NC 27411. E-mail: ylin@ncat.edu

Some of these authors have employed different mesoscale models to study OP under idealized upstream conditions for a conditionally unstable flow passing over an idealized bell-shaped mountain. These authors showed that mountains influence as well as induce precipitation through the alteration of thermodynamical, microphysical and dynamical structures of the impinging air masses. In this study, we are particularly interested in the heavy OP induced or enhanced by the orography when a tropical cyclone (TC) passes over a mesoscale mountain because it often provides favorable conditions leading to heavy precipitation and the dynamics for this extremely large Froude-number flow is not well understood.

Tropical cyclones impinging on the Appalachians in the United States (e.g., Hurricane Ivan, 2004), the mountainous islands of the Caribbean Sea (e.g., Hurricane Jeanne, 2004), La Réunion and Madagascar islands of the Indian Ocean (e.g., Tropical Cyclone Gamede, 2007), Central Mountain Ranges (CMR) of Taiwan (e.g., Typhoon Morakot, 2009) all resulted in heavy precipitation. The devastating property damage and loss of lives of extreme OP events demand more studies on OP phenomenon in order to improve our preparedness. Although isolated islands have served as subjects to many OP studies, robust quantitative precipitation forecast remains a challenge to the forecast community. Part of the forecasting problem is due to the lack of understanding of combined effects of dynamical, thermodynamical, and microphysical processes on OP.

CL00 determined three moist flow regimes for a conditionally unstable flow over an idealized two-dimensional mesoscale mountain. These regimes are: (I) an upstream propagating convective precipitation system, (II) a quasi-stationary convective system over the mountain peak, and (III) quasi-stationary convective system over the mountain peak and downstream propagating convective system. These regimes were classified based on the magnitude of upstream unsaturated moist Froude number ($F_w=U/N_wh$). Here, U is the basic flow speed, h is the mountain height and N_w is the unsaturated moist Brunt-Väisälä frequency. Increasing rainfall accumulations were observed over the mountain peak or upslope of the terrain in the study as a response to increasing basic wind speed. Chen and Lin (2005) hypothesized that, in addition to the F_w, convective available potential energy *(CAPE)* also influences moist flow regimes. The hypothesis was tested by varying F_w and *CAPE* for a conditionally unstable flow over an idealized 2D mountain. It was found that under low *CAPE* flows, OP can be modulated by large horizontal wind speed. The implication for a tropical cyclone is that the system does not necessarily require high *CAPE* to produce heavy orographic rainfall. However, different combinations of *CAPE* and horizontal wind speed lead to different precipitation types. Chen et al. (2008) further investigated moist flow regimes by considering the effects of the mountain aspect ratio (*h/a*) and F_w using 2D idealized WRF model simulations. A moist unstable flow with higher Froude number (i.e., higher wind speed with fixed buoyancy frequency and mountain height) was observed to produce heavy stratiform rainfall. In addition, a slow moving quasi-stationary convective system also generated high precipitation over the mountain.

Recent studies of orographic effects on precipitating clouds showed that OP involves complicated microphysical and dynamical interactions (Houze 2012). In reality, these interactions have major roles in the enhancement and diminishment of OP. Lin (2007) lists the following cases to illustrate these interactions: "(a) increase of upward transport of water vapor and hydrometeors; (b) enhancing the accretion processes through forced lifting and the reduction of the lifting condensation level over the mountain surface; (c) changes in microphysical pathways in the production of precipitation; (d) interception of hydrometeors by a mountain surface at a higher level; (e) changes in the horizontal advection scale of air motion compared to the time scale for microphysical process; (f) changes in precipitation efficiency; (g) enhanced evaporation over the downslope with the addition of adiabatic warming; and (h) small-scale heavy orographic precipitation via turbulent motion."

This research follows the approach taken by CL00, which relies on studying the basic control parameters that affect orographic flow and precipitation in a conditionally unstable flow. In this study, we will concentrate on the variations in *U*, intending to investigate dynamical and microphysical structures of OP modified by hurricane-strength wind as well as low-wind over an idealized two-dimensional mesoscale mountain.

2. NUMERICAL EXPERIMENTAL DESIGN

This research employs the Weather Research and Forecasting (WRF v3.5) model for numerical simulations. The numerical experiments are designed by utilizing the WRF test case of two-dimensional flow over hills and following the experimental design of CL00. Horizontal grid spacing (Δx and Δy) is 1 km while the vertical grid spacing (Δz) is ~0.5 km up to 12 km then stretched to about 2 km near the domain top at 25 km. A sponge layer is added from 16 km to the model top to absorb wave energy generated in the physical domain. The total grid points of the domain in the *x, y,* and *z* directions are 1007 x 4 x 51. The model time step (Δt) is 1 s. Each simulation is run for 12 h and the simulated fields are output at every 6 min.

West-east lateral boundaries are chosen to be open so that numerical disturbances can propagate out of the domain. Periodic boundary condition is chosen in the south-north direction. The 1.5-order turbulent kinetic energy (TKE) closure is activated. Rotational effects are ignored by setting the Coriolis parameter to zero. Cumulus, planetary boundary layer (PBL), and radiation parameterizations are deactivated for all simulations, similar to previous idealized simulations. The Goddard Lin-Farley-Orville (Lin et al. 1983; Tao and Simpson 1993) microphysics parameterization scheme is used to explicitly resolve microphysical processes and precipitation.

The most notable difference in model setup between CL00 and this study is that the former uses the Advanced Regional Prediction System (ARPS) model (Xue et al. 2000) with a coarser horizontal grid resolution ($\Delta x = \Delta y = 2.5$ km), which specifies 403 grid points in the *x*-direction. Even though CL00 uses higher resolution in the lower layer, such as 200 m at the surface stretching up to 1100 m at the model top, we found there are only minor qualitative differences between of our simulations and those of CL00.

A bell-shaped idealized two-dimensional mountain is impulsively introduced at the model initialization time. The mountain profile is identical to CL00 and is given below which is denoted by the bold curve on top of the gray region of Fig. 3,

$$h(x) = \frac{h}{(x/a)^2 + 1} \tag{1}$$

where *h* and *a* are the mountain height (2 km) and half-width (30 km), respectively. Both of them are fixed in all simulations.

Figure 1 shows the idealized conditionally unstable Weisman and Klemp (1982) sounding which is used to initialize the simulations. Its analytical expressions can be found in the original paper and CL00. Several important properties of this sounding are: 1) westerly wind profile is uniform throughout the vertical domain. 2) *CAPE* is about 1900 J/kg and the equilibrium level (*EL*) extends up to near tropopause (11.5 km) which is favorable for the production of deep convective cells. 3) Lifted condensation level (*LCL*) is at about 1 km and the level of free convection (*LFC*) is at 1.6 km which is below the 2 km mountain height. This means the mountain can mechanically trigger convection upon interacting with the incoming unstable flow. 4) The surface temperature is near 27 ^{o}C, the freezing level is located at near 3.5 km, and 14 g/kg of water vapor is available up to slightly above the *LCL*. The sounding parameters are calculated using the *getcape.F* script provided in the Cloud Model 1 (CM1) (Bryan and Fritsch 2002) based on the surface parcel ascent. Most-unstable parcel and mixed-layer (lowest 500 m) parcel options yield *CAPE* values of about 2300 J/kg and 1950 J/kg, respectively.

3. RESULTS

Using the experimental design described in the previous section, five numerical simulations are performed (Table 1). Verification analysis will be provided in the next section for the first four cases. More detailed analyses will follow on the high wind Case TC in the following section.

3.1. Verification of Chu and Lin's (2000) Study

The main objective of this section is to verify the 2D moist flow regimes of CL00. This analysis establishes a basis to relate *U* and OP in a conditionally unstable atmosphere. CL00 mainly used the time evolutions of surface wind and rainwater mixing ratio in determining the three moist flow regimes, this study classifies flow regimes based on the time and spatial distribution of precipitation. CL00 conducted 19 simulations (cf. Table 2), whereas this study runs only four cases to perform the verification analysis.

The left panels in Fig. 2 show the horizontal distribution of 12 h total rainfall for each case, while the right panels show the time evolution of hourly rain rate within the whole simulation domain. These two representations of precipitation give a clear idea as to how each case is identified as a different flow regime.

In Case B1, a precipitation peak over the upwind side of the barrier and an upstream propagating convective system is identified. When the *U* is increased to 4.25 m s^{-1}, a similar regime behavior is observed as in Case B1. The system produces slightly more precipitation over the mountain and the peak of the precipitation shifts closer to the mountain top, compare to CL00. The upstream extent of the precipitation is over -400 km in the B1, however, B2 upstream precipitation extent is around -300 km due to the weakened density current strength. This case was classified as Regime II in CL00 which is different than the results presented here. The difference between these two findings is mostly because B2 is a transitional regime and reproducing this stationary convective regime requires additional numerical settings tuning which are not considered in this study. When the *U* is further increased to 10 m s^{-1}, cold pool formation on the upstream of the mountain completely vanishes and majority of the precipitation is concentrated over the mountain. The peak precipitation is almost at the mountain summit. Although this case show the behavior of a Regime II, the corresponding Hovmöller diagram presents a downstream precipitation mode, however much weaker comparing to the stationary system. At 20 m s^{-1} the stationary precipitation becomes more focused over at the mountain. Comparing to the previous case the downstream precipitation mode tends to be slightly larger. Both of these last cases are classified as Regime III which is consistent with the CL00's results.

Figure 3 shows the 12 h total precipitation distribution for all four cases described and additionally for the Case TC. The combined plot clearly shows that as the *U* is increased, the maximum total rainfall increases and the location of the precipitation maximum shifts closer to the mountain peak. With the increasing wind speed, advection time gets smaller; therefore precipitation shifts from upwind side to mountain peak and falls towards downwind of the mountain. This can be explained with the fact that hydrometeors do not have enough time to develop and precipitate on the upslope, but rather being advected towards the downwind slope, as the wind speed is increased. Looking at the peak precipitation values on the left panels of Fig. 2 and Table 1, it is clear that OP is proportional to the *U* due to the orographic lifting. However, no such proportionality exists between the *U* and maximum rain rates (right panels of Fig. 2). This is explained by the fact that updrafts are not only driven by orographic forcing but also by the amount of the instability available in the environment which is essentially represented by *CAPE* (Lin et al. 2001, Lin 2007). The maximum rain rate values indicate that even the lowest wind speed can produce locally heavy precipitation in a short time period which may cause flash flooding.

In addition to the total rainfall distributions, Fig. 3 includes the slope of the mountain which is illustrated by the thin red line. The slope reaches its maximum at -17 km and its minimum at 17 km. The maximum and minimum values of the slope are 0.043 and -0.043, respectively. All cases except case TC show a uni-modal precipitation distribution pattern. It is not clear at this point if the location of maximum/minimum slope can be related, if so how.

3.2. High Wind Case

In this section, we investigate the detailed precipitation amount and distribution of the high wind case, namely the Case TC. Basic flow speed of a 50 m s^{-1} is well-representative of TC wind strengths which corresponds to a hurricane category of 2-3. The 12h precipitation total (Fig. 4) shows a bi-modal distribution with the first peak is located at the mountain summit, and the second peak, which is about 2/3 of the first precipitation maximum, is located about 40 km downwind of the summit. In the bottom panel, Hovmöller evolution of the hourly precipitation rate is shown over the 12 h period and within the domain of [-200, 200 km]. The convective system produces two local hourly precipitation maxima, which the former is at about 2 h and the latter is at about 8 h into the simulation within 10 km downwind and peak of the mountain. There is another relatively smaller maximum near hour 9 and over 40-50 km downwind of the mountain which appears to be responsible for the second peak shown in Fig. 4a. Majority of the OP reaches the surface within about x = -10 to 100 km of the mountain.

Figures 5 to 8 show three-hourly evolutions of dynamical, thermodynamical and microphysical fields from Case TC simulation. Figure 6 is the same as Fig. 5 except it zooms into the domain, i.e. 12 km and [-100, 100 km] in the vertical and horizontal respectively. Deep convective cells are produced as a result of strong orographic lifting within the vicinity of the mountain up to 6 h into the simulation. There are still patterns of concentrated (up/downward) regions over the upslope at hour 9, however a part of the system is advected towards downslope and much deeper cells form further upwind side of the mountain resulted from wave breaking aloft. At 12 h convective cells are about 50 km and more on the downwind side, which are triggered by a hydrostatic jump. Cloud and hydrometeor formation are focused within the vicinity of the mountain and lee-side except at 12 h. After 9 h, the cloud envelope starts propagating upstream to about -400 km. Additionally, the precipitating deep convective system is detached from the lee-side component.

Figure 7 and 8 shows evolution of precipitating hydrometeor fields similar to Figs. 5 and 6. Hydrometeors are concentrated within the mountain, mostly on the lee side; up to 9 h, then all hydrometeors are advected upstream. Rain formation is confined in the lower layer up to about 3-4 km while the upper layer is mostly dominated by the snow and graupel. This is expected as the freezing level is noted around 3.5 km above the ground as indicated by the sounding (Fig. 3). Although there is no clear correspondence between the regions of updraft cells and hydrometeor active regions, microphysical activities are clearly noted from the potential temperature contours as a result of latent heat release. The depth of convective cells, which is mostly containing the snow and graupel, is higher in early hours of the simulation comparing to later hours. Hydrometeors are advected further upstream at 12 h however the contribution of these cells on precipitation is negligible comparing to the precipitation accumulated over the mountain.

To investigate the evolution of the precipitating system from 9 to 12 h, hourly outputs of relative humidity, 2D wind vectors and potential temperature are plotted in Fig. 9. At 9 h and later, wave breaking and very strong downdrafts are evident and these result in a concentrated region of dry air downwind of the mountain. Cellular convective cells occur at 10 h while they move upstream and redevelop further until the end of the simulation. Our explanation of why these cells do not contribute to the surface precipitation is that relative humidity values within these cells drop below 20-40 % thus causing evaporation of hydrometeors before reaching the ground.

3.3. Microphysics

In this section, the distribution of individual microphysical species is investigated. For this purpose, vertically integrated and time accumulated distributions of cloud, rain, ice, snow, graupel (q_c, q_r, q_i, q_s, q_g) as well as water vapor and all species combined (q_v and q_{ALL}) are plotted in Fig. 10 over [-100, 100 km] zoomed-in model domain. Although how much each hydrometeor species contributes to precipitation is not quantitatively determined, it can be seen that the graupel contributes the most to the precipitation, out of precipitation forming species. Given the warm surface sounding structure and the concentrated regions of cold (snow, graupel) hydrometeors in the layer above 4 km as shown in Fig. 8, *the microphysical pathway of this contribution occurs mostly through the graupel to rain transformation (melting) mechanism*. Although there are noticeable amount of rain/snow/graupel over the upslope, due to the strong basic flow, the majority of hydrometeors are advected to the mountain peak and mostly on the lee side, consistent with the precipitation distribution (Fig. 4).

From the mass conservation point of view, heavy hydrometeor active regions (particularly graupel) are corresponding to the regions of water vapor consumption. Plotting of all species combined is a useful representation as this approach helps determining the amount of precipitation is produced within the OP system. If one were to assume a hypothetical straight line indicating the total amount of available moisture content within the model, assuming there is no precipitation forcing, then precipitation efficiency could be determined by measuring the distance from this base line to q_{ALL}. In a separate study, we will be considering this type of approach and systematically investigate precipitation efficiency based on the variations with respect to the *U*.

4. CONCLUDING REMARKS

Two-dimensional simulations have been conducted to examine dynamical and microphysical process evolutions as well as precipitation structure in a conditionally unstable flow over an idealized mountain. In the first part of the study, two out of three regimes of CL00, namely Regimes I and III, which are corresponding to low and high wind speeds, have been reproduced using WRF simulations. Due to transient nature of the Regime II, which is a flow with intermediate wind speed, this flow regime has not been verified with the same flow settings used in CL00.

Maximum of the accumulated OP is found to respond linearly to the increasing *U* by analyzing four simulations from the first part and the hurricane strength wind cases. This proportionality is explained as a result of the orographic lifting and *U* relation. Contrary to the accumulated maximum, hourly precipitation rate maximum does not show a linear dependence to the variation in *U*. This is explained by the fact that part of the upward motion is contributed by the available instability (i.e., *CAPE*) within the incoming flow. In fact, the lowest *U* (2.5 m s^{-1}, Case (B1)) produces heaviest precipitation rate among all the simulations. The implication of this finding is *a moderately unstable slow-moving system can result in local flash flooding*.

Second part of the study extends on the first part by analyzing a hurricane strength wind speed simulation over an idealized mountain. As evidenced from the first part, this case produces the heaviest precipitation accumulation at the end of 12 h simulation. Precipitation shows a bi-modal distribution with the stronger peak located over the mountain summit and weaker peak located about 40 km downstream of the mountain. Under 50 m s^{-1} westerly flow speed, hydrometeors do not have enough time to mature to precipitation sizes at the upwind side of the mountain and they are advected towards downwind to contribute in surface precipitation. The 12 h total and vertically integrated horizontal distributions of hydrometeors show that *graupel contributes most significantly in the precipitation, indicating the important roles played by the ice phase microphysical processes*.

Precipitation system exhibits an upstream propagation after 9 hours of simulation. Detailed analyses of hourly field cross-sections reveal that these *cellular convective cells located upstream of the mountain are produced by orographic forcing rather than triggered by density current*. Moreover, the contribution of the convective cells to precipitation upstream of the mountain is negligible comparing to the primary precipitation, which is concentrated over the mountain.

An example of a simple analysis of the impacts of *U* on OP efficiency is provided in the last part of the study. However, the degree to which precipitation is enhanced under differing flow speed conditions awaits further examination. In addition, microphysical pathway analysis is required to determine the most dominant microphysical process for each flow speed and their contribution to surface precipitation. The second part of this paper is going to investigate the variations in CAPE on the production and evolution of OP.

Acknowledgments: This research was supported by the National Science Foundation Awards AGS-1265783 and OCI-1126543.

5. REFERENCES

Bryan, G. H., and J. M. Fritsch, 2002: A benchmark simulation for moist nonhydrostatic numerical models. *Mon. Wea. Rev.*, **130**, 2917-2928. doi: 10.1175/1520-0493(2002)130<2917:ABSFMN>2.0.CO;2

Chen, S.-H., and Y.-L. Lin, 2005: Effects of moist Froude number and CAPE on a conditionally unstable flow over a mesoscale mountain ridge. *J. Atmos. Sci.*, **62**, 331-350. doi: 10.1175/JAS-3380.1

Chen, S.-H., Y.-L. Lin, and Z. Zhao, 2008: Effects of unsaturated moist Froude number and orographic aspect ratio on a conditionally unstable flow over a mesoscale mountain. *J. Meteor. Soc. Japan*, **80**, 99-118. doi: 10.2151/jmsj.86.353

Chu, C.-M., and Y.-L. Lin, 2000 (CL00): Effects of orography on the generation and propagation of mesoscale convective systems in a two-dimensional conditionally unstable flow. *J. Atmos. Sci.*, **57**, 3817-3837. doi: 10.1175/1520-0469(2001)057<3817:EOOOTG>2.0.CO;2

Colle, B. A., 2004: Sensitivity of orographic precipitation to changing ambient conditions and terrain geometries: An idealized modeling perspective. *J. Atmos. Sci.*, **61**, 588-606. doi: 10.1175/1520-0469(2004)061<0588:SOOPTC>2.0.CO;2

Houze, R. A., Jr., 2012: Orographic effects on precipitating clouds. *Rev. Geophys.*, **50**, RG1001, doi:10.1029/2011RG000365

Huang, Y.-C., and Y.-L. Lin, 2014: A study on the structure and precipitation of Morakot (2009) induced by the Central Mountain Range of Taiwan. *Meteor. Atmos. Phys.*, **123**, 115-141. doi: 10.1007/s00703-013-0290-4.

Lin, Y.-L., 2007: *Mesoscale Dynamics*. Cambridge University Press, 630 pp.

Lin, Y.-L., R. D. Farley, and H. D. Orville, 1983: Bulk parameterization of the snow field in a cloud model. *J. Appl. Meteor.*, **22**, 1065–1092. doi: 10.1175/15200450(1983)022<1065:BPOTSF>2.0.CO;2

Miglietta, M. M., and R. Rotunno, 2009: Numerical simulations of conditionally unstable flows over a mountain ridge. *J. Atmos. Sci.*, **66**, 1865–1885. doi: 10.1175/2009JAS2902.1

Miglietta, M. M., and R. Rotunno, 2010: Numerical simulations of low-CAPE flows over a mountain ridge. *J. Atmos. Sci.*, **67**, 2391–2401. doi: 10.1175/2010JAS3378.1

Miglietta, M. M., and R. Rotunno, 2014: Numerical simulations of sheared conditionally unstable flows over a mountain ridge. *J. Atmos. Sci.*, 7**1**, 1747–1762. doi: 10.1175/JAS-D-13-0297.1

Tao, W.-K., and J. Simpson, 1993: Goddard Cumulus Ensemble Model. Part I: Model description. *Terr. Atmos. Ocean. Sci.*, **4**, 35-72.

Weisman, M. L., and J. B. Klemp, 1982: The dependence of numerically simulated convective storms on vertical wind shear and buoyancy. *Mon. Wea. Rev.*, **110**, 504–520. doi: 10.1175/1520-0493(1982)110<0504:TDONSC>2.0.CO;2

Xue, M., K. K. Droegemeier, and V. Wong, 2000: The Advanced Regional Prediction System (ARPS) - A multiscale nonhydrostatic atmospheric simulation and prediction tool. Part I: Model dynamics and verification. *Meteor. Atmos. Physics.*, **75**, 161-193. doi: 10.1007/s007030070003

Table 1: Summary of the basic flow speed (U), unsaturated moist Froude number (F_w), unsaturated moist Brunt-Väisälä frequency (N_w) is assumed as 0.006 s^{-1}), estimated orographic lifting (w_{oro} with maximum mountain slope = 0.043), maximum rain rate (R_{max}), location of maximum total rainfall (X_{tmax}), and maximum total rainfall (R_{tmax}) are listed.

Case	U (*m/s*)	F_w ($U / N_w h$)	$w_{oro} \approx U \partial h / \partial x$ (*m/s*)	R_{max} (*mm/h*)	X_{tmax} (*km*)	R_{tmax} (*mm*)
B1	2.5	0.21	0.11	26.9	-33	52.7
B2	4.25	0.35	0.18	21.5	-9	55.9
B3	10	0.83	0.43	16.3	-2	114.5
B4	20	1.67	0.87	21.7	-2	148.4
TC	50	4.17	2.16	25.2	1	214.5

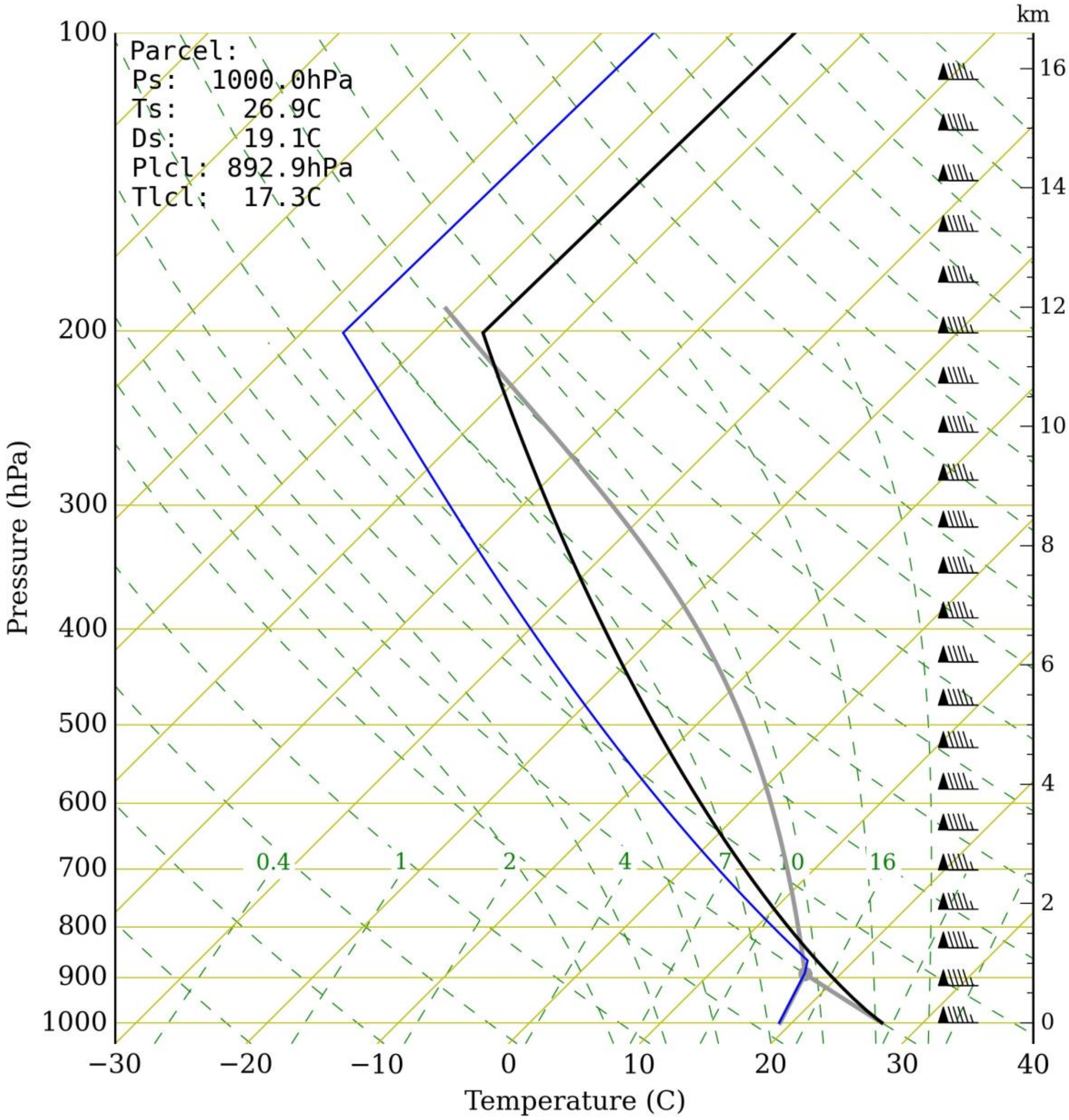

Fig. 1: Skew-T diagram of the Weisman and Klemp (1982) sounding used for all the simulations, except for Case TC with U = 50 m s^{-1}.

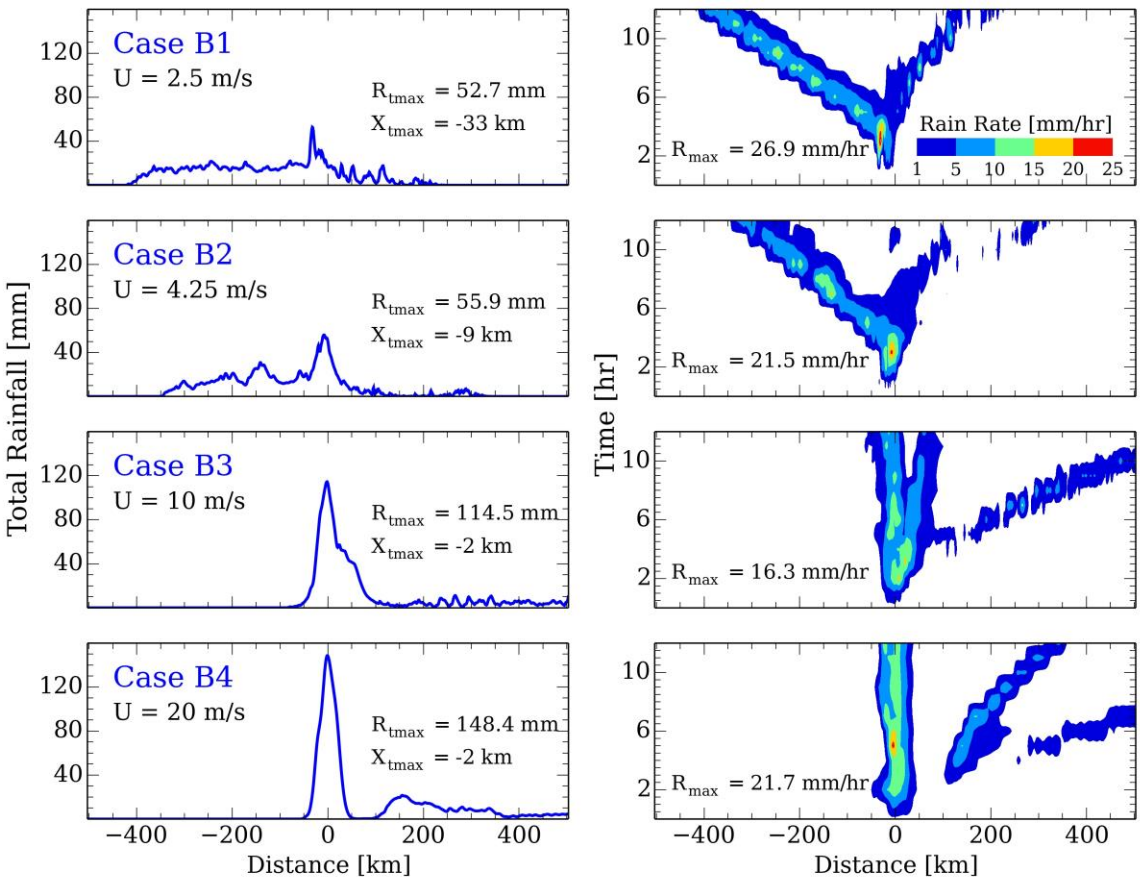

Fig. 2: Total rainfall distributions (12 h) and Hovmöller diagrams of hourly rain rates are shown for the four simulated cases in the left and right panels, respectively. R_{tmax} (maximum total rainfall), X_{tmax} (location of maximum total rainfall) and R_{max} (maximum rain rate) are indicated in the panels. The colorbar in the top-right panel is representative of all cases shown on the right panels.

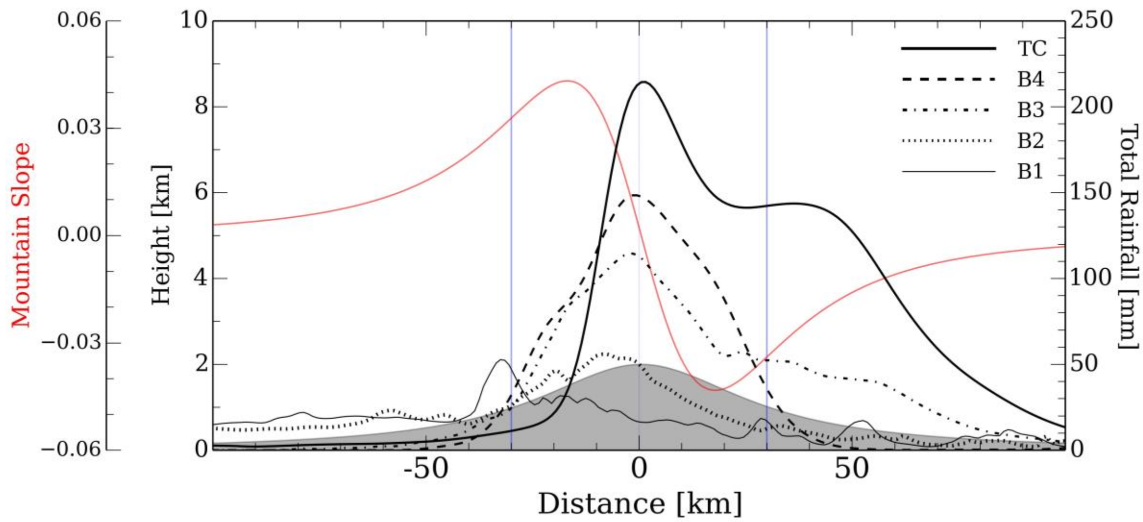

Fig. 3: Total rainfall distributions (12 h) over the zoomed domain of [-100, 100 km] for the five numerical experiments as indicated by the different line types. The thin red line shows the mountain slope which belongs to the leftmost detached axis. The idealized mountain profile is also shown. Thin blue lines correspond to the mountain half-width which is kept at 30 km for all experiments.

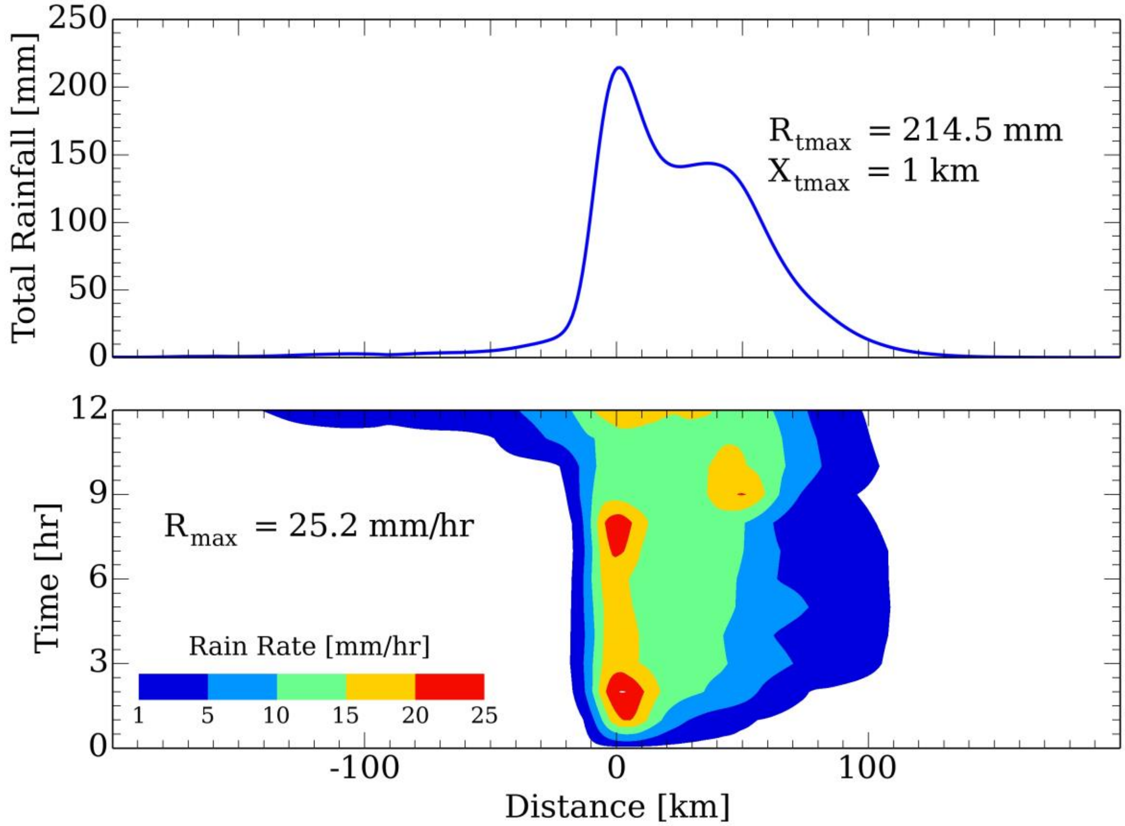

Fig. 4: Total rainfall distributions (12 h) and Hovmöller diagrams of hourly rain rates for Case TC in the top and bottom panels, respectively. Rainfall characteristics are indicated as in Fig. 2. Note that the plotting domain is shown at [-200, 200 km] range.

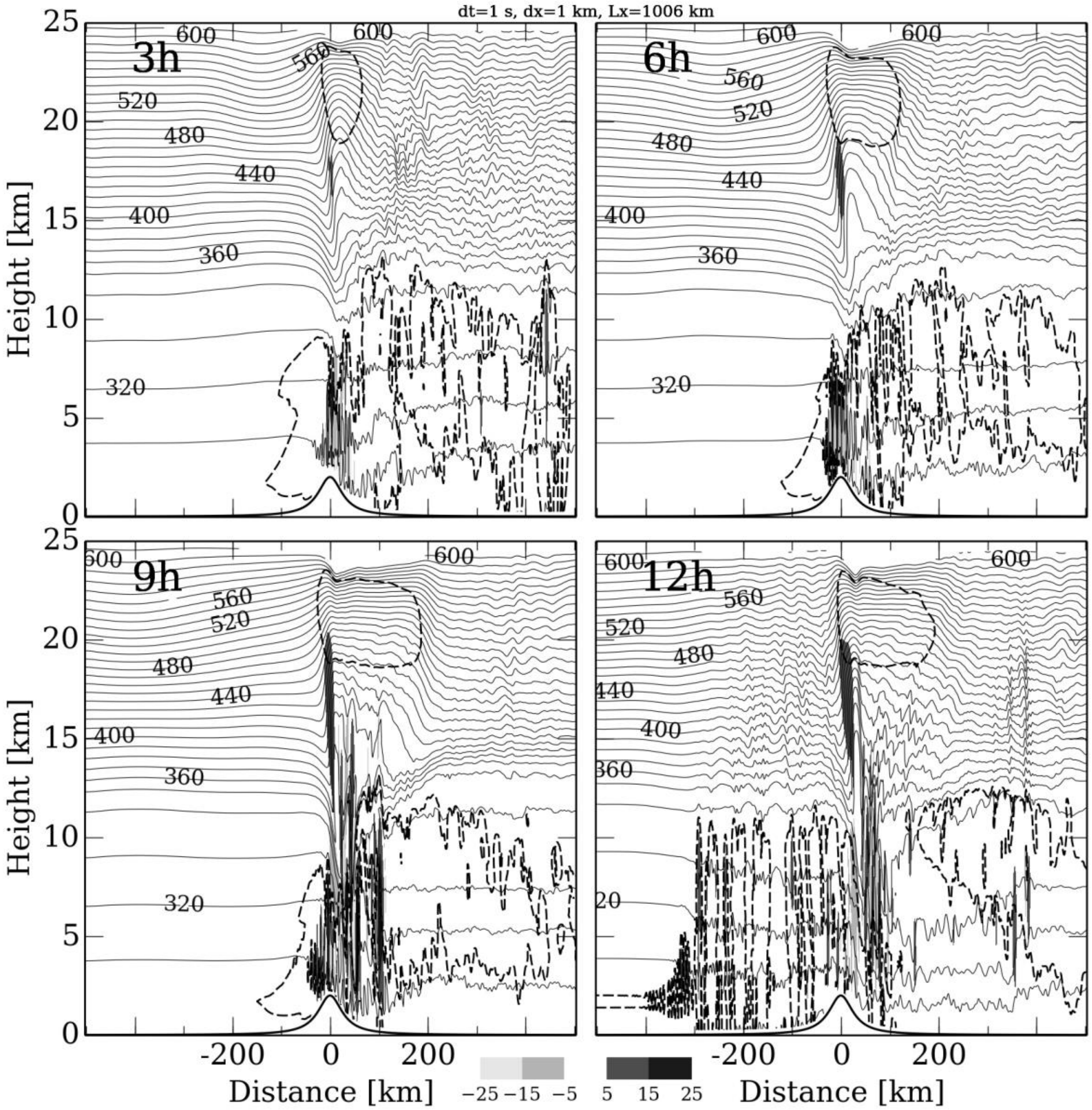

Fig. 5: Three hourly evolutions of the potential temperature (thin line contours, plotted at every 10 K), vertical velocity (filled gray contours in the range of -25 to 25 m/s with darker grays indicate updraft and lighter grays indicate downdraft regions), cloud envelope (thick dashed line, contoured for the combined hydrometeor values which are greater than 0.05 g/kg). The plotting area shows the whole domain.

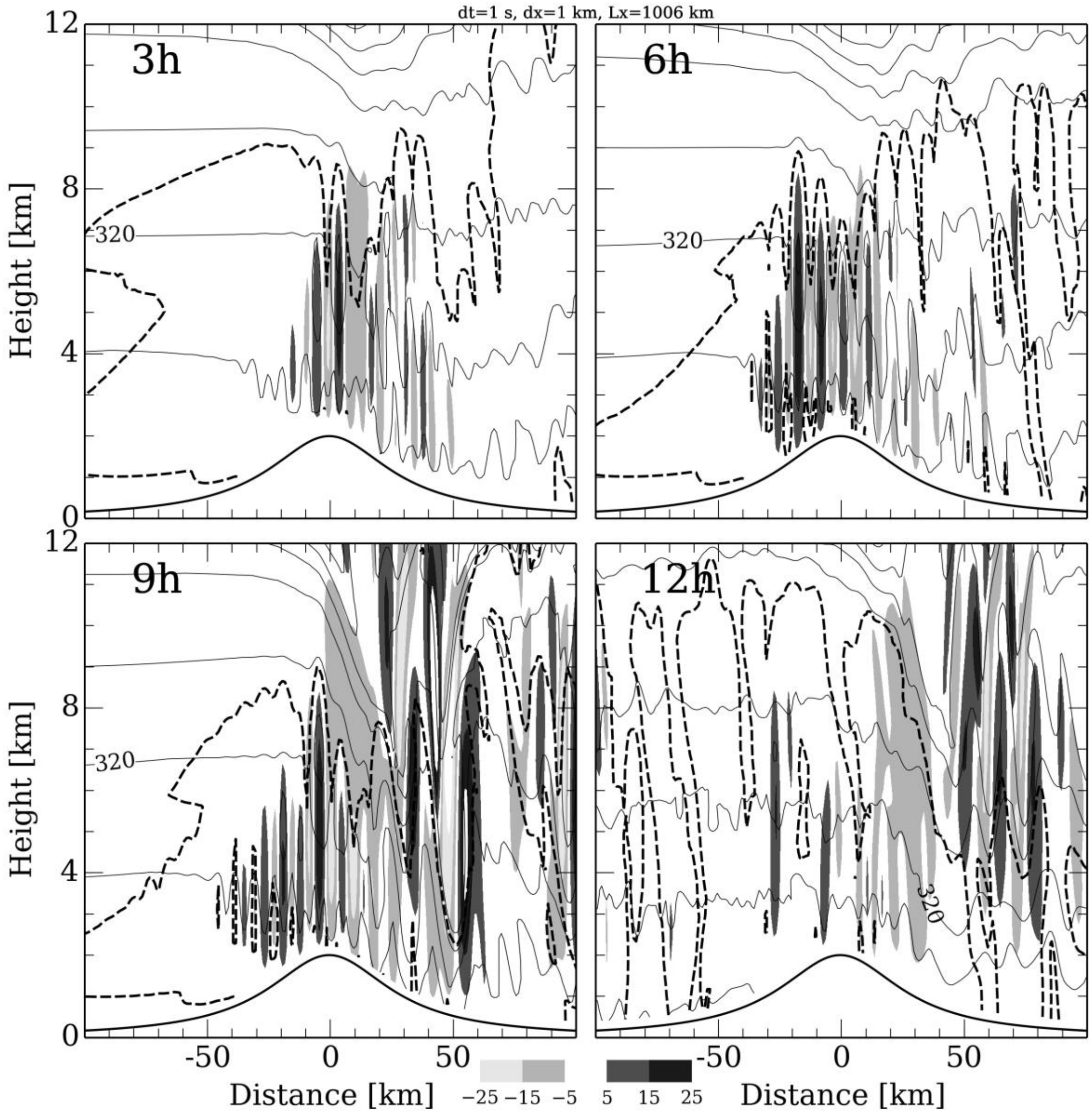

Fig. 6: Same as Fig. 5 except the plotting domain is zoomed in to 12 km and [-100, 100 km] in the vertical and horizontal, respectively.

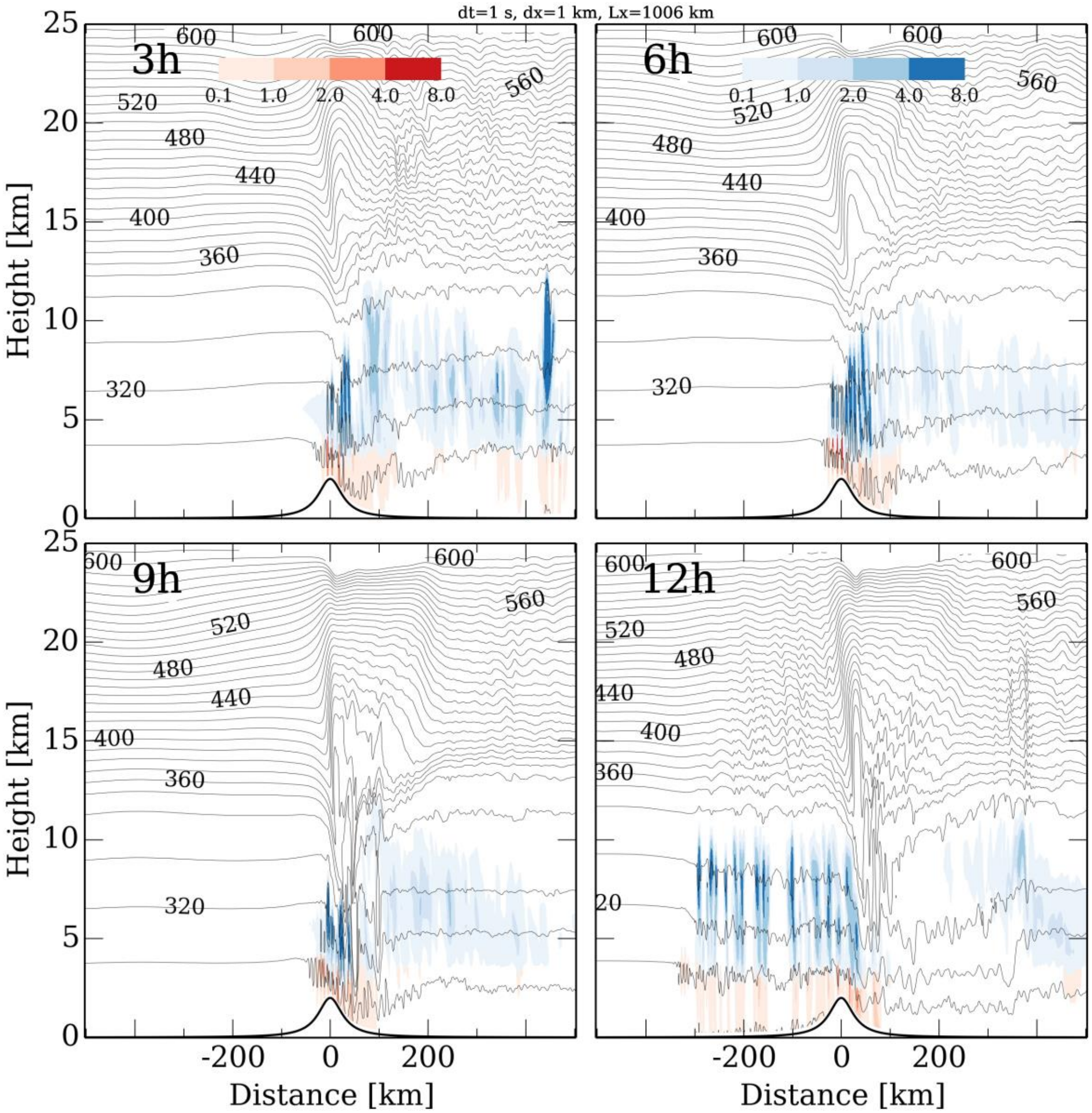

Fig. 7: Three hourly evolutions of warm (q_r: red filled contours between 0.1 and 0.8 g/kg) and cold (q_s+q_g; blue filled contours between 0.1 and 8.0 g/kg) hydrometeors. Potential temperatures (thin line contours, plotted at every 10 K) are also shown. The plotting area shows the whole vertical and horizontal simulation domain.

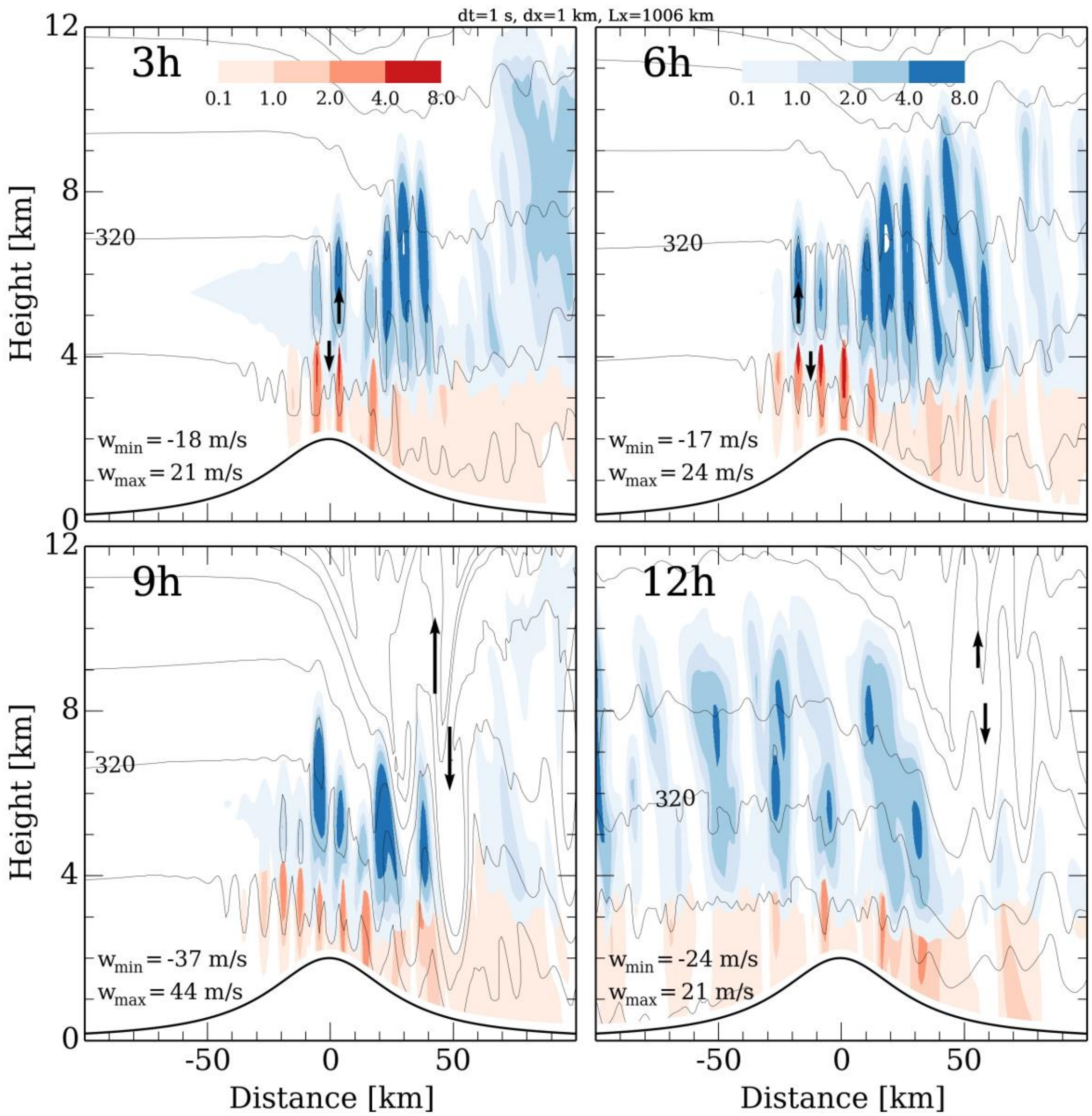

Fig 8: Same as Fig. 7, except the plotting domain is zoomed in to 12 km and [-100, 100 km] in the vertical and horizontal, respectively. Bold thick arrows indicate the maximum location of updraft and downdrafts. Their numerical values are provided in the lower-left regions of each panel.

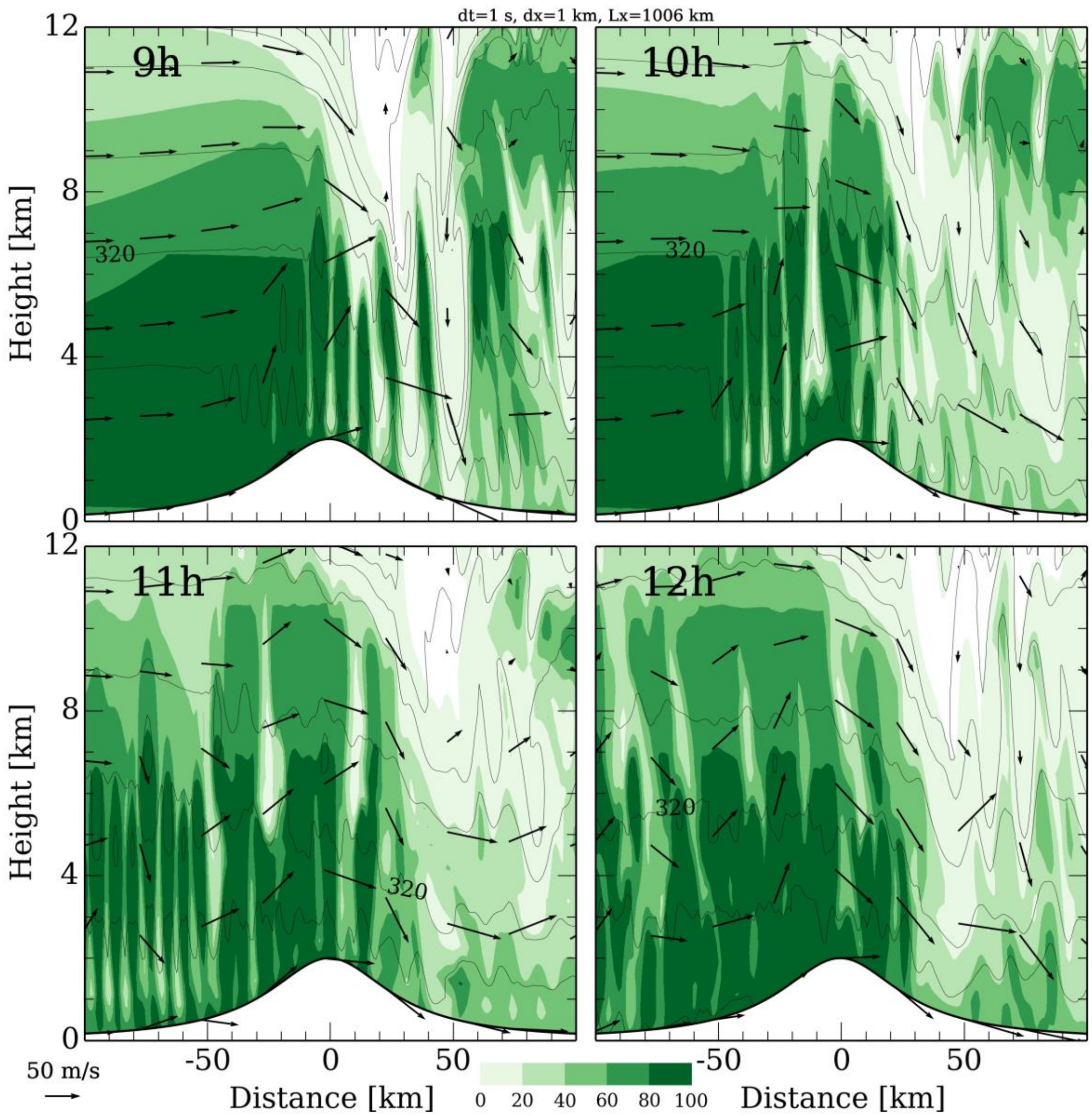

Fig. 9: Hourly evolutions of the relative humidity with respect to water (green filled contours shaded at every 20 %), potential temperature (thin line contours, plotted at every 10 K), and wind vector fields. The plotting area shows 12 km and [-100, 100 km] of the vertical and horizontal simulation domain, respectively, for the 9-12 h interval.

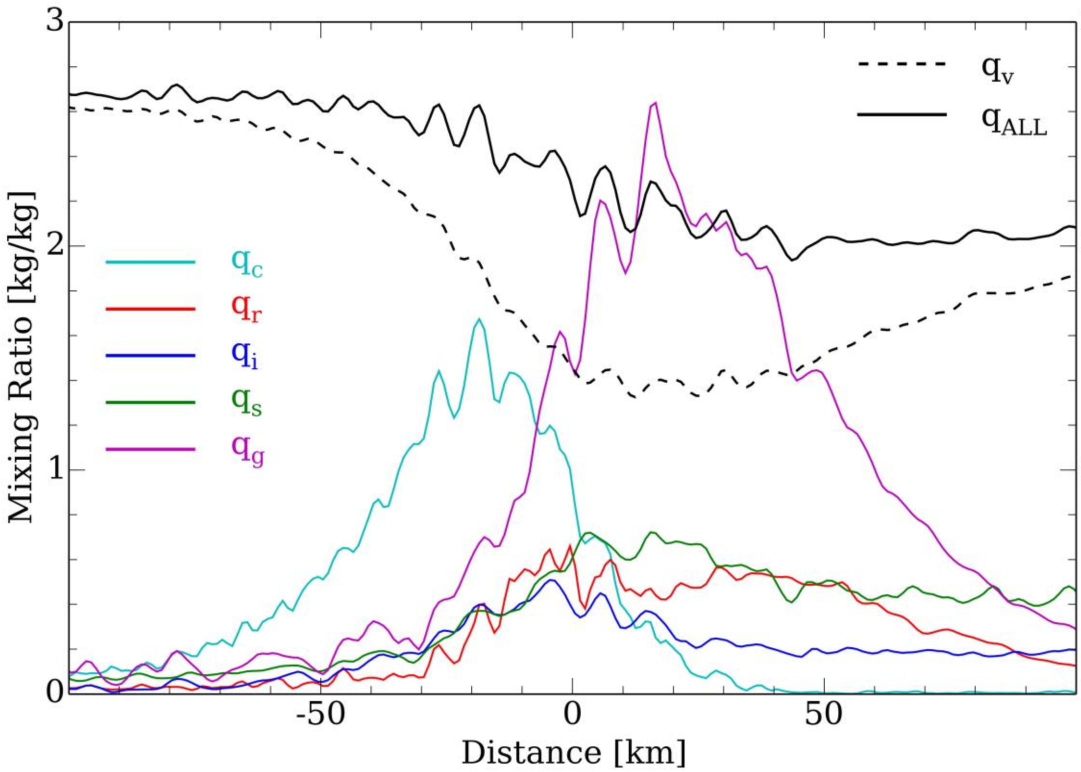

Fig. 10: Vertically integrated and time accumulated distributions of mixing ratios of individual microphysical hydrometeors. The left axis belongs to the five individual species as indicated by the color line legend. The right axis shows the distribution vapor mixing ratio (q_v, dashed line) and all microphysical species combined (q_{ALL}, solid line). Note that horizontal domain shows the range of [-100, 100 km] as in Fig. 8.